



# CHORUS

This is the accepted manuscript made available via CHORUS. The article has been published as:

## Dirac states in the noncentrosymmetric superconductor BiPd

Arindam Pramanik, Ram Prakash Pandeya, Denis V. Vyalikh, Alexander Generalov, Paolo Moras, Asish K. Kundu, Polina M. Sheverdyeva, Carlo Carbone, Bhanu Joshi, A.

Thamizhavel, S. Ramakrishnan, and Kalobaran Maiti

Phys. Rev. B **103**, 155401 — Published 1 April 2021

DOI: [10.1103/PhysRevB.103.155401](https://doi.org/10.1103/PhysRevB.103.155401)

# Dirac states in a non-centrosymmetric superconductor, BiPd

Arindam Pramanik<sup>1</sup>, Ram Prakash Pandeya<sup>1</sup>, D. V. Vyalikh<sup>2,3</sup>, Alexander Generalov<sup>4</sup>, Paolo Moras<sup>5</sup>, Asish K. Kundu<sup>5</sup>, Polina M. Sheverdyayeva<sup>5</sup>, Carlo Carbone<sup>5</sup>, Bhanu Joshi<sup>1</sup>, A. Thamizhavel<sup>1</sup>, S. Ramakrishnan<sup>1</sup>, and Kalobaran Maiti<sup>1\*</sup>

<sup>1</sup>*Department of Condensed Matter Physics and Materials Science, Tata Institute of Fundamental Research, Homi Bhabha Road, Colaba, Mumbai - 400005, India*

<sup>2</sup>*Donostia International Physics Center (DIPC),*

*20018 Donostia San Sebastián, Basque Country, Spain*

<sup>3</sup>*IKERBASQUE, Basque Foundation for Science, 48013, Bilbao, Spain*

<sup>4</sup>*MAX IV Laboratory, Lund University, PO Box 118, 22100, Lund, Sweden*

<sup>5</sup>*Istituto di Struttura della Materia, Consiglio Nazionale delle Ricerche, I-34149 Trieste, Italy*

Quantum materials having Dirac fermions in conjunction with superconductivity is believed to be the candidate materials to realize exotic physics as well as advanced technology. Angle resolved photoemission spectroscopy (ARPES), a direct probe of the electronic structure, has been extensively used to study these materials. However, experiments often exhibit conflicting results on dimensionality and momentum of the Dirac Fermions (e.g. Dirac states in BiPd, a novel non-centrosymmetric superconductor), which is crucial for the determination of the symmetry, time-reversal invariant momenta and other emerging properties. Employing high-resolution ARPES at varied conditions, we demonstrated a methodology to identify the location of the Dirac node accurately and discover that the deviation from two-dimensionality of the Dirac states in BiPd proposed earlier is not a material property. These results helped to reveal the topology of the anisotropy of the Dirac states accurately. We have constructed a model Hamiltonian considering higher-order spin-orbit terms and demonstrate that this model provides an excellent description of the observed anisotropy. Intriguing features of the Dirac states in a non-centrosymmetric superconductor revealed in this study expected to have significant implication in the properties of topological superconductors.

## INTRODUCTION

Recent times has seen the emergence of a new class of insulating materials, which are topological in nature. While the bulk of these materials is insulating, surface harbours partially filled (metallic) spin-split two dimensional bands with cone like structure (Dirac cone) arising due to the topological nature of the bulk bands. Bi<sub>2</sub>Se<sub>3</sub> is one of the most studied materials in this category[1], where the surface states and its evolution with impurities have been studied extensively [2–4]. The pool of topological materials have been enriched via discovery of Dirac Fermions as the surface states in superconductors such as BiPd [5–7],  $\beta$ -PdBi<sub>2</sub> [8], Cu<sub>x</sub>Bi<sub>2</sub>Se<sub>3</sub> [9], Sr<sub>x</sub>Bi<sub>2</sub>Se<sub>3</sub> [10, 11], etc. Among these topological materials, BiPd grabbed much attention as it stabilizes in noncentrosymmetric monoclinic structure( $P2_1$ ) known as  $\alpha$ -BiPd and superconductivity appears below 3.8 K[12–14]. Above 483 K, it undergoes polymorphic transition from  $\alpha$ -BiPd to orthorhombic  $\beta$ -BiPd (space group -  $Cmc2_1$ ).

Due to the absence of inversion symmetry, (010) and (0 $\bar{1}$ 0) faces of BiPd are inequivalent and the binding energy at the Dirac nodes on respective faces are also different. Interestingly, the twinning in the samples allows photoemission experiments to capture properties of both the surfaces simultaneously; while the Dirac bands on (010) face appear clearly in the experimental spectra, bands on (0 $\bar{1}$ 0) face are often weak and appear in the immediate vicinity of the bulk states. Benia *et al.*[5] pointed out that the Dirac states in BiPd may not have topolog-

ical origin as these are found in density functional calculations both with and without spin-orbit (SO) coupling. On the other hand, spin-resolved photoemission measurements have confirmed the spin-polarization of these states, which is a signature of topological behavior[7]. It is to note here that spin-polarized surface states are also observed in systems with heavy elements due to strong Rashba coupling.

Despite several studies, even the identification of the location of Dirac node and the dimensionality of the Dirac states are outstanding issues. Thirupathaiiah *et al.*[6] reported this band to be found at  $\bar{\Gamma}$  (Brillouin zone center). However, Yaresko *et al.* have shown the Dirac states to be positioned at  $\bar{S}$ , a high-symmetry point at the surface Brillouin zone boundary based on their detailed density functional theoretical (DFT) calculations [15]. In addition to this conflicting results on location of the Dirac node, Thirupathaiiah *et al.*[6] proposed three dimensional nature of the Dirac states depicted by an energy gap at the Dirac node varying with  $k_z$ ; although the repetitive nature of the gap as a function of  $k_z$  was not observed. However, the DFT results characterize Dirac states as two dimensional surface states.[5, 7] We carried out high-resolution angle-resolved photoemission spectroscopic (ARPES) measurements at carefully chosen experimental conditions and discover that the Dirac states are truly two dimensional; the anomalies reported earlier arose due to the sample alignment used in those experiments. Furthermore, we find that the anisotropy in the dispersion of the Dirac bands reported earlier [5, 6]

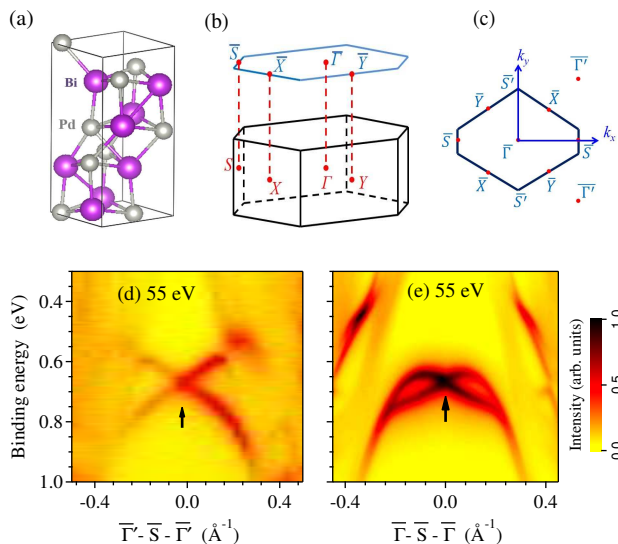


FIG. 1. (a) Unit cell of BiPd in real space. (b) Bulk and (c) surface Brillouin zones. ARPES data (d) along  $\bar{\Gamma}-\bar{S}-\bar{\Gamma}$  and (e)  $\bar{\Gamma}-\bar{S}-\bar{\Gamma}$  vectors. Dirac point is identified with an arrow and the  $k$ -axis is shifted to make  $\bar{S}$ -point as zero.

appears far away from the Dirac node. We have constructed a model Hamiltonian considering higher-order spin-orbit terms, which provides a good description of all the features of the Dirac bands observed experimentally.

## EXPERIMENT

High-quality single crystals of BiPd were grown using modified Bridgman method. Crystal structure of the sample was determined via analysis of powder  $x$ -ray diffraction pattern and good crystallinity has been ensured employing Laue diffraction experiments. The lattice parameters found in the study correspond to the monoclinic structure as reported elsewhere.[12] Magnetization measurements exhibit a superconducting transition at 3.8 K. ARPES measurements were performed at Diamond Light Source, United Kingdom and Elettra, Italy. At Diamond Light Source, experiments were carried out at I05 beamline [16] at a temperature of 10 K, base pressure of  $5 \times 10^{-11}$  torr and energy resolution of 5 meV. Measurements at Elettra were done at VUV beamline at a temperature of 25 K, base pressure of  $6 \times 10^{-11}$  torr and energy resolution of 10 meV.

## RESULTS AND DISCUSSIONS

The crystal unit cell of BiPd is shown in Fig. 1(a) exhibiting a non-centrosymmetric structure. In Figs. 1(b) and 1(c), we show the bulk Brillouin zone (BZ) and its

projection on the surface, respectively. The axis system is defined by aligning  $k_x$  along  $\bar{\Gamma}-\bar{S}$  direction and  $k_y$  along  $\bar{\Gamma}-\bar{S}'$  direction. Photoemission spectra along two directions are shown in Figs. 1(d) and 1(e) with the Dirac point appearing at 0.66 eV binding energy shown using an arrow. The analysis of the data as discussed in Fig. 2 suggests that the Dirac point is positioned at  $\bar{S}$  point in the surface Brillouin zone, which is about  $0.73 \text{ \AA}^{-1}$  away from the  $\bar{\Gamma}$  point; in the figure, the  $k$ -axis is shifted to make it zero at the Dirac node. While the bands along  $\bar{\Gamma}-\bar{S}-\bar{\Gamma}$  exhibit spin splitting varying monotonically with momentum, the momentum dependence of the spin-splitting along  $\bar{\Gamma}-\bar{S}-\bar{\Gamma}$  is non-linear; it increases to a maximum near momentum of  $0.1 \text{ \AA}^{-1}$  away from  $\bar{S}$  and then decreases revealing strong anisotropy of the Dirac Fermionic bands as discussed earlier [5, 6].

To investigate the dimensionality of the Dirac states, we acquired spectra at various photon energies, which helps to decide surface or bulk nature of the bands. In Figs. 2(a)(i)-(iii), we show a set of spectra along with corresponding energy distribution curves (EDC) in Figs. 2(b)(i)-(iii). Second set of spectra is displayed in Figs. 2(c)(i)-(iii) with corresponding EDCs in Figs. 2(d)(i)-(iii). Pieces cut from the same single crystal were used to obtain these two sets of spectra. A close inspection reveals interesting differences between the two sets. In the first set (the sample position optimized using 74 eV photon energy), as the photon energy is lowered, the Dirac cone becomes more asymmetric and the bands do not cross each other. The energy gap at the Dirac node was derived by fitting two peaks in the EDC (blue curves in Figs. 2(b)) across the node. The gap increases as the probing energy is lowered. The second set of the spectra were collected after optimizing the sample position at 35 eV photon energy and the Dirac node could be captured just by optimization of the sample alignment. Curiously, the second set exhibits an opposite trend of the gap at the Dirac node; the energy gap continuously increases with the increase in photon energy across 74 eV as manifested clearly in the EDCs (blue curves in Fig. 2(d)). In this case, the dispersion of the Dirac bands remains symmetric over the energy range studied. In Figs. 2(e) & 2(f), we show the derived energy gaps of the first and second sets, respectively exhibiting opposite trend. We note here that the Dirac bands shown in Fig. 1(d) and 1(e) collected at 55 eV photon energy after optimizing the sample position also show distinct Dirac node. All these results suggest that the  $k$ -point at the Dirac node may be different from  $\bar{\Gamma}$ -point; change in photon energy moves the  $k$ -point away from Dirac node.

In order to probe this further, we consider that the  $\bar{\Gamma}-\bar{S}$  vector makes an azimuthal angle,  $\theta_1$  with the vertical axis and tilt angle,  $\theta_2$ ; here, the photoemission plane is a horizontal plane as shown in the Appendix. Clearly, the presence of finite  $\theta_1$  will manifest as an asymmetry in the cone structure as the probed  $k$ -vector does not pass

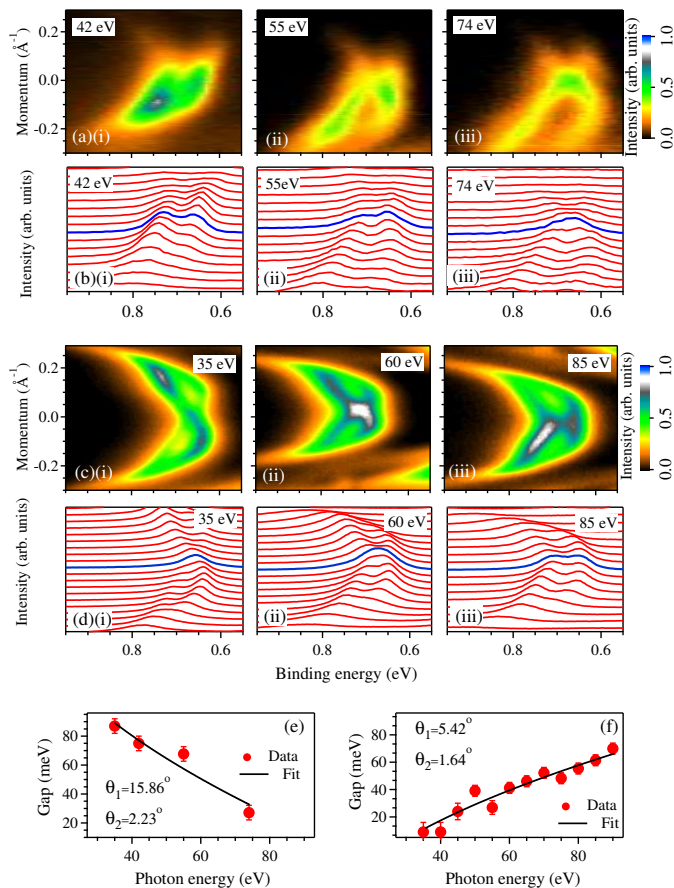


FIG. 2. (a)(i)-(iii) ARPES data collected along  $\bar{\Gamma} - \bar{S} - \bar{\Gamma}$  direction and (b)(i)-(iii) the corresponding energy distribution curves (EDCs) after normalizing the sample position using 74 eV photon energy. (c)(i)-(iii) Similar second set of ARPES data collected after sample normalization using 35 eV photon energy and (d)(i)-(iii) corresponding EDCs. Blue lines mark the EDCs passing through the Dirac node. The energy gaps derived at the Dirac node at  $\bar{S}$ -point from (e) the first and (f) the second set of the spectra. Black lines superimposed over the data points represent the estimated energy gaps considering  $\bar{\Gamma} - \bar{S}$  vector makes an azimuthal angle,  $\theta_1$  and tilt angle,  $\theta_2$  as shown in the Appendix.

through the Dirac node. This argument is verified from the values of  $\theta_1$  obtained from fittings in Figs. 2(e)& 2(f); the first set of spectra (see Fig. 2(a)) exhibit strong asymmetry and could be captured with a higher value of  $\theta_1$  compared to the second set shown in Fig. 2(b). Derived values of  $\theta_2$  are also listed in the figures. Excellent representation of the experimental results establishes that the gap at the Dirac node is not the property of the material but arises due to the sample alignment and that the Dirac node is not located at  $\bar{\Gamma}$ . Zero gap within the experimental error can be obtained for both sets of data at all probing energies once the fitted curve is subtracted

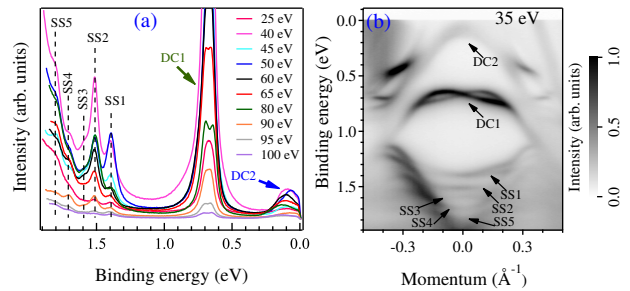


FIG. 3. (a) EDCs passing through the Dirac node are plotted for multiple photon energies ranging from 25 eV to 100 eV. DC1 and DC2 are the Dirac cones on 010 and  $0\bar{1}0$  surfaces, respectively. DC1 exhibits splitting into two peaks where the alignment of the sample is away from  $\bar{S}$ -point due to the change in photon energy. SS1-SS5 label the surface states at higher binding energies. (b) A representative spectrum at 35 eV shows all the observed surface states of BiPd.

from the measured gap. This is manifested in the experimental data; the sample realignment at different photon energies leads to reduction of the energy gap to zero. For example, the data in Figs. 1(d) and 1(e) exhibits a distinct Dirac node for photon energy of 55 eV although the spectra collected using other setup for the same photon energy show non-zero gap. This is in addition to the data in Figs. 2(a)(iii) and 2(c)(i) for 74 eV and 35 eV, respectively. This establishes the finite momentum at the Dirac node and two dimensional nature of the Dirac states as there is no observable variation of the bands with the photon energy.

Identification of the correct momentum and dimensionality of the Dirac node is important as the symmetry of the states depends on the momentum of the Dirac states and dimensionality provides the behavior of the states. For the ease of presentation and/or calculations, sometimes, a nonprimitive unit cell is used to derive the electronic structure of a system. Such consideration introduces additional folding of the energy bands and one needs to unfold them to identify their momentum as discussed earlier[15]. On the experimental front, the way to identify the correct momentum and dimensionality of the eigenstates is to map the Fermi surface at multiple photon energies, presumably at photon energies corresponding to non-equivalent  $k$ -point and then take the correct cut. The experimental data and ensuing analysis presented here provide the momentum and dimensionality of the Dirac Fermions consistent with the theoretical results [15].

Besides the widely discussed Dirac states, we discover few more two-dimensional states lying at higher binding energies. In Fig. 3(a), we show the EDCs at various photon energies taken across the Dirac node. DC1 is the Dirac state under investigation. DC2 shown in the inset of Fig. 3(a) is the Dirac cone on  $(0\bar{1}0)$  surface [5]. In addition, few other states labeled as SS1-SS5 are seen to

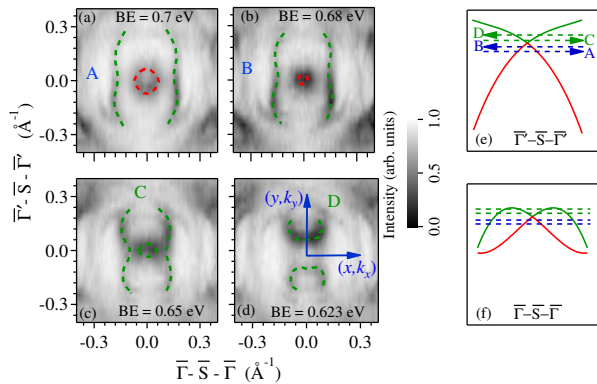


FIG. 4. Constant-energy contours in the  $xy$ -plane at binding energies (a) 0.7 eV, (b) 0.68 eV, (c) 0.65 eV and (d) 0.623 eV obtained from the ARPES data at 55 eV photon energy as shown in Fig. 1. The binding energy positions of the contours are labeled as A, B, C and D and shown schematically in (e) along the  $k$ -vector,  $\bar{\Gamma}^v - \bar{S} - \bar{\Gamma}^v$  and (f) along the  $k$ -vector,  $\bar{\Gamma} - \bar{S} - \bar{\Gamma}$ . Green and red colors identify the contours derived from green and red colored energy bands. Cartesian coordinate system is shown in (d);  $(x, k_x)$  lies along  $\bar{\Gamma} - \bar{S} - \bar{\Gamma}$ .

be positioned at fixed binding energies even as the photon energy is varied over a large range. Since these bands are not observed in the theoretical results [15] for the bulk band structure, we attribute these two-dimensional states as surface states. Understanding of the nature of these bands requires further theoretical studies including various surface effects.

We now address the issue of anisotropy of the Dirac bands; such anisotropy has also been reported in other materials. For example,  $\text{Bi}_2\text{Te}_3$ [17, 18] and  $\text{Bi}_2\text{Se}_3$ [19, 20] are two prominent cases of this class. There are other cases too, such as  $\text{Ru}_2\text{Sn}_3$ [21],  $\beta\text{-Bi}_4\text{I}_4$ [22],  $\beta\text{-HgS}$ [23],  $\beta\text{-Ag}_2\text{Te}$  [24], Au film grown on  $\text{Ag}(111)$ [25], Ag film grown on Au (111)[25] etc. Anisotropy in these systems is attributed to the symmetries at the surfaces. In Figs. 4(a) - 4(d), we show the constant-energy contours of BiPd taken across the Dirac states. Energy positions of the contours are shown using schematics in Figs. 4(e) and 4(f) with dashed lines. Each constant-energy map consists of two contours. Green and red colors are used to identify the contours with the energy bands above and below the Dirac point. Shape of all the contours exhibits the twofold rotational symmetry of the crystal belonging to  $C_2$  point group. Interestingly, the inner contour near the nodal point is isotropic (cut A, B & C) and gradually evolves into a twofold symmetric curve far away from the nodal point. At the top of the Dirac cone, the contour evolves into two disjoint segments (cut D). Further, we notice that the top and bottom portions of the outer contour (green) are missing in all the cuts including D. This scenario is consistent with the observation

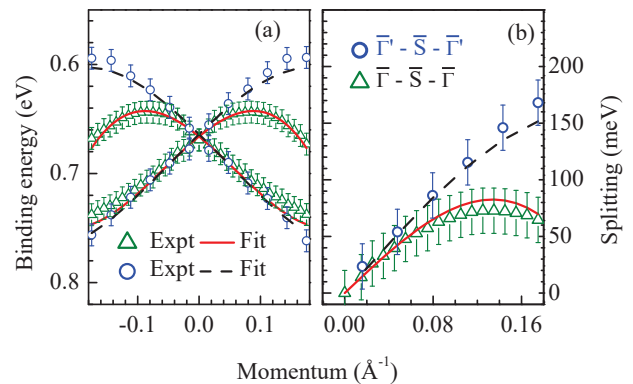


FIG. 5. (a) Dispersion along  $\bar{\Gamma}^v - \bar{S} - \bar{\Gamma}^v$  (blue open circles) and  $\bar{\Gamma} - \bar{S} - \bar{\Gamma}$  (green open triangles) derived from EDCs. Solid and dashed lines represent the fits based on the eigenvalue equation 1. (b) Spin splitting along  $\bar{\Gamma} - \bar{S} - \bar{\Gamma}$  (green open triangles) and  $\bar{\Gamma}^v - \bar{S} - \bar{\Gamma}^v$  (blue open circles). Solid and dashed lines represent the fits based on the eigenvalue equation. 1.

in Fig. 1(d), where, the surface bands merge with the bulk band along  $\bar{\Gamma}^v - \bar{S} - \bar{\Gamma}^v$  resulting into an incomplete contour. The twofold rotational symmetry implies that electrons are subject to the effects of crystal potential. Benia *et al.* argued that a twofold rotational symmetry in the Rashba coupling strength at the surface is responsible for this anisotropic band dispersion [5]. However, it is difficult to capture the non-parabolic dispersion along  $\bar{\Gamma} - \bar{S} - \bar{\Gamma}$  (Fig. 1 (e)) as well as the contour shapes shown in Fig. 4 using this scenario. Moreover, a  $C_2$  symmetric Rashba coupling, which is first order in momentum  $(k_x, k_y)$ , will produce two fold symmetric contours near the node unlike the circular contours seen here.

Experimentally observed dispersions of the Dirac bands along two orthogonal directions are shown in Fig. 5(a). It is evident in the figure that although the dispersions are different far away from the node, they are very similar near the node as found in the constant energy contours of Fig. 4. Such a behavior suggests importance of higher order spin-orbit terms [26, 27]. Considering the  $C_2$  point group of the material and time reversal symmetry, we derive the Hamiltonian up to the third order term in momentum. The choice of the axes are shown in Fig. 1, where the  $x$ -axis lies along  $\bar{\Gamma} - \bar{S} - \bar{\Gamma}$  direction. A model Hamiltonian with the  $\bar{S}$  point as the reference point is constructed as follows.

$$H = A(\vec{k})\sigma_x + B(\vec{k})\sigma_y + C(\vec{k})\sigma_z + D(\vec{k})I_{2 \times 2} \quad (1)$$

where  $\sigma_x, \sigma_y$ , and  $\sigma_z$  are Pauli matrices and  $I_{2 \times 2}$  is a  $2 \times 2$  identity matrix.  $A, B$ , and  $C$  are functions of lattice momenta,  $k_x$  and  $k_y$ , with the following forms.

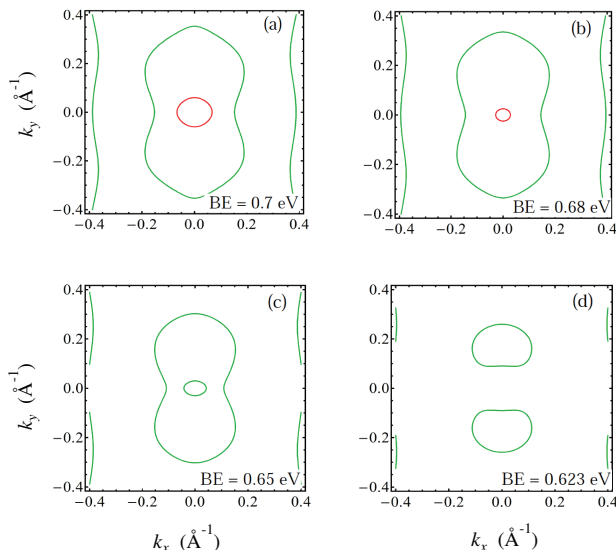


FIG. 6. Contours simulated at (a) 0.7 eV, (b) 0.68 eV, (c) 0.65 eV and (d) 0.623 eV binding energies using the Hamiltonian in equation. 1. Parameters used for the simulations are listed in [28]. Colors (red or green) of contours are in accordance with Fig. 4.

$$\begin{aligned}
 A(\vec{k}) &= c_1 k_x + c_2 k_y + c_3 k_x k_y^2 + c_4 k_y k_x^2 + c_5 k_x^3 + c_6 k_y^3 \\
 B(\vec{k}) &= c_7 k_x + c_8 k_y + c_9 k_x k_y^2 + c_{10} k_y k_x^2 + c_{11} k_x^3 + c_{12} k_y^3 \\
 C(\vec{k}) &= 0 \\
 D(\vec{k}) &= E_0 + c_{13} k_x^2 + c_{14} k_y^2 + c_{15} k_x k_y
 \end{aligned}$$

Clearly, for small  $k$ -values, contributions from higher order terms becomes insignificant and one can get essentially an isotropic description from the above Hamiltonian. By fitting the band dispersions along various  $k$ -directions, one can estimate the parameters adequately to derive the band structure [28]. We discuss a typical case below.

Band dispersion and spin splitting extracted from EDCs from the spectrum at 55 eV are shown by symbols in Fig. 5(a) and 5(b), respectively. Spin splitting along  $\bar{S} - \bar{\Gamma}'$  direction is represented by open circles and along  $\bar{S} - \bar{\Gamma}$  direction, it is open triangles. The spin splitting along  $\bar{S} - \bar{\Gamma}'$  varies almost linearly with momentum as expected for Rashba split parabolic bands. Along  $\bar{S} - \bar{\Gamma}$ , away from  $\bar{S}$  point, the bands deviate from the expected parabolic dispersion. The splitting varies linearly with momentum close to  $\bar{S}$  point and at large momentum, effect of higher order terms takes over. Fitting of all the curves are done using expressions derived from equation 1 and in each case, good quality of fitting is achieved for momentum region away from the influence of bulk bands.

To confirm that the obtained description reproduce the experimental results shown in Fig. 4, we simulated the

constant energy maps using above description. In Fig. 6, we show the contours at binding energies similar to that shown in Fig. 4. Note that since the size of the model Hamiltonian is  $2 \times 2$ , it describes only the spin-split Dirac like states and does not capture the merger of the Dirac states with the bulk bands along  $\bar{S} - \bar{\Gamma}'$  direction. Hence, it provides closed contours as expected for surface states in a scenario where merging to the bulk bands is absent. The shapes of the contours provide an excellent description of the experimentally observed scenario around  $\bar{S}$ -point. It is to note here that spin-orbit coupling in solid can have contributions ( $= -\frac{e\hbar}{(2mc)^2} \sigma \cdot (E(r) \times p)$ ;  $E(r)$  is the electric field) in addition to the atomic values. This is more so in a material having no center of symmetry as reported earlier [29]. Thus, the origin of the above behavior may be attributed to the strong spin-orbit coupling in this non-centrosymmetric solid, BiPd.

It has been shown that higher order spin orbit coupling gives rise to out-of-plane spin polarization in systems such as  $\text{Bi}_2\text{Se}_3$  [26, 30],  $\text{Bi}_2\text{Te}_3$  [18, 26],  $\beta\text{-Ag}_2\text{Te}$  [24] etc. The surface states in BiPd will, however, not possess out-of-plane spin component. Spin splitting term containing  $\sigma_z$ , which leads to the out-of-plane spin polarization, is absent in the Hamiltonian (see equation. 1) owing to the  $C_2$  symmetry of the system. Hence, the spin polarization of the states will lie in  $k_x - k_y$  plane [31].

## CONCLUSIONS

In summary, we studied the Dirac states in a non-centrosymmetric superconductor, BiPd. High-quality of the sample and high-resolution of the ARPES technique employed in this study helped to reveal subtle features in the electronic structure. Our experimental results helped to identify the momentum of the Dirac node and establish the two dimensional character of the Dirac states resolving the outstanding disputes on these two issues. This study brings out the importance of deriving correct experimental geometry to reveal experimental results related to the properties of materials, in particular, the cases where the point of interest is not the center of the Brillouin zone ( $\bar{\Gamma}$ -point). This is crucial for the identification of the symmetry properties, time reversal invariant momenta and their implication in various other exoticity of the material. In addition, we discover several other surface states at binding energies higher than the Dirac point revealing complexity of the system. Since the Rashba term alone cannot adequately capture the experimental results, we constructed a model Hamiltonian including spin-orbit coupling terms of higher-order in momentum. Our model provide an excellent description of the anisotropy of the Dirac states. The necessity of the higher-order terms reveals importance of the absence of inversion symmetry in the electronic properties of such systems.

## ACKNOWLEDGEMENTS

Authors acknowledges financial support from the Department of Atomic Energy, Govt. of India under the project no. 12-R&D-TFR-5.10-0100, Diamond Light Source for beamtime at the beamline I05 under proposal SI11512. DVV acknowledges support from the Spanish Ministry of Economy (No. MAT-2017-88374-P). KM acknowledges financial support from DAE, Govt. of India under the DAE-SRC-OI Award program, and Department of Science and Technology, Govt. of India under J. C. Bose Fellowship program.

---

\* Corresponding author: kbmaiti@tifr.res.in

- [1] H. Zhang, C. X. Liu, X. L. Qi, X. Dai, Z. Fang, and S. C. Zhang, *Nat. Phys.* **5**, 438-442 (2009).
- [2] Y. L. Chen, J. H. Chu, J. G. Analytis, Z. K. Liu, K. Igarashi, H. H. Kuo, X. L. Qi, S. K. Mo, R. G. Moore, D. H. Lu, M. Hashimoto, T. Sasagawa, S. C. Zhang, I. R. Fisher, Z. Hussain, and Z. X. Shen, *Science* **329**, 659 (2010).
- [3] D. Kong, J. J. Cha, K. Lai, H. Peng, J. G. Analytis, S. Meister, Y. Chen, H. J. Zhang, I. R. Fisher, Z. X. Shen, and Y. Cui, *ACS Nano* **5**, 46984703 (2011).
- [4] D. Biswas, S. Thakur, K. Ali, G. Balakrishnan, and K. Maiti, *Sci. Rep.* **5**, 10260 (2015); D. Biswas, S. Thakur, G. Balakrishnan, and K. Maiti, *Sci. Rep.* **5**, 17351 (2015); D. Biswas and K. Maiti, *EPL* **110**, 17001 (2015); D. Biswas and K. Maiti, *J. Elec. Spec. Relat. Phenom.* **208**, 90 (2016).
- [5] H. M. Benia, E. Rampi, C. Trainer, C. M. Yim, A. Maldonado, D. C. Peets, A. Stöhr, U. Starke, K. Kern, A. Yaresko, G. Levy, A. Damascelli, C. R. Ast, A. P. Schnyder, and P. Wahl, *Phys. Rev. B* **94**, 121407(R) (2016).
- [6] S. Thirupathiah, S. Ghosh, R. Jha, E.D.L. Rienks, K. Dolui, V.V. R. Kishore, B. Büchner, T. Das, V.P.S. Awana, D.D. Sarma, and J. Fink, *Phys. Rev. Lett.* **117**, 177001 (2016).
- [7] M. Neupane, N. Alidoust, M. M. Hosen, J. X. Zhu, K. Dimitri, S. Y. Xu, N. Dhakal, R. Sankar, I. Belopolski, D. S. Sanchez, T. R. Chang, H. T. Jeng, K. Miyamoto, T. Okuda, H. Lin, A. Bansil, D. Kaczorowski, F. Chou, M. Zahid Hasan, and T. Durakiewicz, *Nat. Commun.* **7**, 13315 (2016).
- [8] M. Sakano, K. Okawa, M. Kanou, H. Sanjo, T. Okuda, T. Sasagawa, and K. Ishizaka, *Nat. Commun.* **6**, 8595 (2015).
- [9] L. A. Wray, S. Y. Xu, Y. Xia, Y. S. Hor, D. Qian, A. V. Fedorov, H. Lin, A. Bansil, R. J. Cava, and M. Z. Hasan, *Nat. Phys.* **6**, 855-859 (2010).
- [10] Shruti, V. K. Maurya, P. Neha, P. Srivastava, and S. Patnaik, *Phys. Rev. B* **92**, 020506(R) (2015).
- [11] C. Q. Han, H. Li, W. J. Chen, F. Zhu, M. Y. Yao, Z. J. Li, M. Wang, B. F. Gao, D. D. Guan, C. Liu, C. L. Gao, D. Qian, and J. F. Jia, *Appl. Phys. Lett.* **107**, 171602 (2015).
- [12] B. Joshi, A. Thamizhavel, and S. Ramakrishnan, *Phys. Rev. B* **84**, 064518 (2011).
- [13] M. Mondal, B. Joshi, S. Kumar, A. Kamlapure, S. C. Ganguli, A. Thamizhavel, S. S. Mandal, S. Ramakrishnan, and P. Raychaudhuri, *Phys. Rev. B* **86**, 094520 (2012).
- [14] Z. Sun, M. Enayat, A. Maldonado, C. Lithgow, E. Yelland, D. C. Peets, A. Yaresko, A. P. Schnyder, and P. Wahl, *Nat. Commun.* **6**, 6633 (2015).
- [15] A. Yaresko, A. P. Schnyder, H. M. Benia, C. M. Yim, G. Levy, A. Damascelli, C. R. Ast, D. C. Peets, and P. Wahl, *Phys. Rev. B* **97**, 075108 (2018).
- [16] M. Hoesch, T. K. Kim, P. Dudin, H. Wang, S. Scott, P. Harris, S. Patel, M. Matthews, D. Hawkins, S. G. Alcock, T. Richter, J. J. Mudd, M. Basham, L. Pratt, P. Leicester, E. C. Longhi, A. Tamai, and F. Baumberger, *Rev. Sci. Inst.* **88**, 013106 (2017).
- [17] Y. L. Chen, J. G. Analytis, J. H. Chu, Z. K. Liu, S. K. Mo, X. L. Qi, H. J. Zhang, D. H. Lu, X. Dai, Z. Fang, S. C. Zhang, I. R. Fisher, Z. Hussain, and Z.-X. Shen, *Science* **325**, 5937 (2009).
- [18] S. Souma, K. Kosaka, T. Sato, M. Komatsu, A. Takayama, T. Takahashi, M. Kriener, K. Segawa, and Y. Ando, *Phys. Rev. Lett.* **106**, 216803 (2011).
- [19] K. Kuroda, M. Arita, K. Miyamoto, M. Ye, J. Jiang, A. Kimura, E. E. Krasovskii, E. V. Chulkov, H. Iwasawa, T. Okuda, K. Shimada, Y. Ueda, H. Namatame, and M. Taniguchi, *Phys. Rev. Lett.* **105**, 076802 (2010).
- [20] T. Valla, Z. H. Pan, D. Gardner, Y. S. Lee, and S. Chu, *Phys. Rev. Lett.* **108**, 117601 (2012).
- [21] Q. D. Gibson, D. Evtushinsky, A. N. Yaresko, V. B. Zabolotnyy, M. N. Ali, M. K. Fuccillo, J. Van den Brink, B. Büchner, R. J. Cava, and S. V. Borisenko, *Sci. Rep.* **4**, 5168 (2014).
- [22] G. Autès, A. Isaeva, L. Moreschini, J. C. Johannsen, A. Pisoni, R. Mori, W. Zhang, T. G. Filatova, A. N. Kuznetsov, L. Forró, W. V. den Broek, Y. Kim, K. S. Kim, A. Lanzara, J. D. Denlinger, E. Rotenberg, A. Bostwick, M. Grioni, and O. V. Yazyev, *Nat. Mater.* **15**, 154 (2015).
- [23] F. Viot, R. Hayn, M. Richter, and J. van den Brink, *Phys. Rev. Lett.* **106**, 236806 (2011).
- [24] W. Zhang, R. Yu, W. Feng, Y. Yao, H. Weng, Xi Dai, and Z. Fang, *Phys. Rev. Lett.* **106**, 156808 (2011).
- [25] R. Requist, P. M. Sheverdyeva, P. Moras, S. K. Mahatha, C. Carbone, and E. Tosatti, *Phys. Rev. B* **91**, 045432 (2015).
- [26] L. Fu, *Phys. Rev. Lett.* **103**, 266801 (2009).
- [27] C. X. Liu, X. L. Qi, H. Zhang, X. Dai, Z. Fang, and S. C. Zhang, *Phys. Rev. B* **82**, 045122 (2010).
- [28] Estimated parameters (units = eV, Å<sup>-1</sup>) found for the description of the dispersion and contours:  $E_0 = -0.66$ ,  $c_{13} = -1.49$ ,  $c_{14} = -0.48$ ,  $c_{15} = 0$ ,  $c_1^2 + c_7^2 = 0.21$ ,  $c_1c_2 + c_7c_8 = 0$ ,  $c_2^2 + c_8^2 = 0.30$ ,  $c_1c_5 + c_7c_{11} = -5.45$ ,  $c_1c_4 + c_7c_{10} + c_2c_5 + c_8c_{11} = 0$ ,  $c_1c_3 + c_7c_9 + c_2c_4 + c_8c_{10} = -1.38$ ,  $c_1c_6 + c_7c_{12} + c_2c_3 + c_8c_9 = 0$ ,  $c_2c_6 + c_8c_{12} = -2.13$ ,  $c_5^2 + c_{11}^2 = 73.67$ ,  $c_4c_5 + c_{10}c_{11} = 0$ ,  $c_4^2 + c_{10}^2 + 2c_3c_5 + 2c_9c_{11} = 50.6$ ,  $c_3c_4 + c_9c_{10} + c_5c_6 + c_{11}c_{12} = 0$ ,  $c_3^2 + c_9^2 + 2c_4c_6 + 2c_{10}c_{12} = -21.6$ ,  $c_3c_6 + c_9c_{12} = 0$ ,  $c_6^2 + c_{12}^2 = 14.97$ .
- [29] A. Pramanik, R. P. Pandeya, K. Ali, B. Joshi, I. Sarkar, P. Moras, P. M. Sheverdyeva, A. K. Kundu, C. Carbone, A. Thamizhavel, S. Ramakrishnan, and K. Maiti, *Phys. Rev. B* **101**, 035426 (2020).
- [30] M. Nomura, S. Souma, A. Takayama, T. Sato, T. Takahashi, K. Eto, K. Segawa, and Y. Ando, *Phys. Rev. B*

89, 045134 (2014).

- [31] D. Yu. Usachov, I. A. Nechaev, G. Poelchen, M. Gttler, E. E. Krasovskii, S. Schulz, A. Generalov, K. Klient, A. Kraiker, C. Krellner, K. Kummer, S. Danzenbcher, C. Laubschat, A. P. Weber, J. Sanchez-Barriga, E. V. Chulkov, A. F. Santander-Syro, T. Imai, K. Miyamoto, T. Okuda, and D. V. Vyalikh, *Phys. Rev. Lett.* **124**, 237202 (2020).

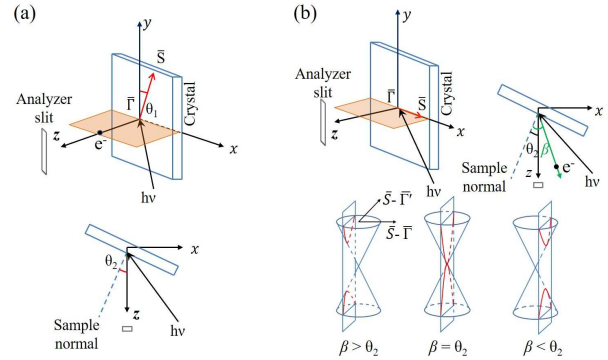


FIG. 7. Schematics of the experimental geometry. (a) The geometry used in the present study where  $\theta_1$  and  $\theta_2$  are in-plane (azimuthal) and out-of-plane (polar) angles, respectively. (b) A special case where the in-plane angle,  $\theta_1 = 90^\circ$ . The angle,  $\beta$  is the emission angle of photoelectrons corresponding to the Dirac node with respect to the sample surface-normal. Conic sections in the lower panel show the expected band dispersions in the spectra for different values of  $\beta$  with respect to  $\theta_2$  due to the change in photon energy keeping the sample orientation unchanged.

## APPENDIX

The experimental geometry involving the sample orientation and the photoemission plane is discussed below. The angle,  $\theta_1$  is defined as the azimuthal angle made by the vector,  $\bar{\Gamma} - \bar{S}$  with the analyzer slit; the analyzer slit is aligned along  $y$  direction. The tilt angle,  $\theta_2$ , is the angle between the analyser and the sample-surface-normal. Depending on the magnitudes of  $\theta_1$  and  $\theta_2$ , different trends of the energy gap at the Dirac node is expected as a function of probing photon energy.

As an example, we consider a less complex scenario in Fig. 7(b);  $\theta_1 = 90^\circ$  &  $\theta_2 \neq 0$ . Here,  $\bar{\Gamma} - \bar{S} - \bar{\Gamma}'$  vector lies along the slit (probed  $k$ -vector). If the Dirac node is located at a finite momentum along the  $\bar{\Gamma} - \bar{S}$  direction, corresponding electrons will emerge at an angle,  $\beta$  with respect to the sample-normal. The magnitude of  $\beta$  depends on the photon energy used for experiments; with the increase of the photon energy,  $\beta$  will reduce. For sufficiently low photon energy,  $\beta$  will be larger than  $\theta_2$ . It becomes equal to  $\theta_2$  at some photon energy and then becomes smaller at higher photon energies. The lower panel of Fig. 7(b) depicts the schematics of the acquired dispersion using conic section. The vertical plane is the plane of constant momentum along  $\bar{\Gamma} - \bar{S}$ , which lies parallel to the analyzer slit. Intersection of this vertical plane and the cone determines the shape of the dispersion (red curves) as seen in the spectra. When  $\beta \neq \theta_2$ , instead of a cone the Dirac state manifests itself as two hyperbolas separated by an energy gap. An ideal cone with a Dirac node is imaged at a particular photon energy when the corresponding  $\beta$  becomes equal to  $\theta_2$ . Earlier ARPES results can be captured excellently well using this description. As a representative case, we analysed the ARPES data of Thirupathiah *et al.* [6] exhibiting identical behavior for  $\theta_2 = 9.6^\circ$  and  $\theta_1 = 90^\circ$ . If  $\theta_1$  is different from  $0^\circ$  or  $90^\circ$ , the cuts on the Dirac cone will not produce hyperbolas symmetrically aligned with respect to the vertical axis. This is the scenario in Fig. 2(a) and 2(b).